

Maoliang Zhang¹, Xian-Gang Xie¹, Wei Liu², Yi Liu¹, Linan Wang¹, Yuji Sano^{3,4}, Yun-Chao Lang¹, Cong-Qiang Liu¹, and Sheng Xu¹

¹School of Earth System Science, Tianjin University

²College of Resources and Environmental Engineering, Inner Mongolia University of Technology

³Marine Core Research Institute, Kochi University

⁴Atmosphere and Ocean Research Institute, The University of Tokyo

January 24, 2024

1
2 **Hydrothermal Degassing Through the Karakoram Fault, Western Tibet: Insights**
3 **Into Active Deformation Driven by Continental Strike-Slip Faulting**

4
5 **Maoliang Zhang^{1,*}, Xian-Gang Xie¹, Wei Liu², Yi Liu¹, Linan Wang¹, Yuji Sano^{3,4}, Yun-**
6 **Chao Lang¹, Cong-Qiang Liu¹, and Sheng Xu^{1,*}**

7
8 ¹School of Earth System Science, Tianjin University, Tianjin 300072, China.

9 ²College of Resources and Environmental Engineering, Inner Mongolia University of
10 Technology, Hohhot 010051, China.

11 ³Marine Core Research Institute, Kochi University, Kochi 783-8502, Japan.

12 ⁴Atmosphere and Ocean Research Institute, The University of Tokyo, Chiba 277-8564, Japan.

13
14 *Corresponding author:

15 Maoliang Zhang (mzhang@tju.edu.cn) and Sheng Xu (sheng.xu@tju.edu.cn)

16
17 **Key Points:**

- 18
- 19 • New He isotope data show that southern Karakoram fault is overwhelmingly dominated
20 by degassing of crustal fluids
 - 21 • A crustal ⁴He- and CO₂-rich fluid reservoir is identified and linked to crustal-scale active
22 deformation driven by strike-slip faulting
 - 23 • Karakoram fault may have limited fluid connections to the mantle and requires further
evaluation based on He isotope and seismic data

Abstract

25 The Karakoram fault is an important strike-slip boundary for accommodating
26 deformation following the India-Asia collision. However, whether the deformation is confined to
27 the crust or whether it extends into the mantle remains highly debated. Here, we show that the
28 Karakoram fault is overwhelmingly dominated by crustal degassing related to a ^4He - and CO_2 -
29 rich fluid reservoir [e.g., He contents up to ~ 1.0 – 1.6 vol.%; $^3\text{He}/^4\text{He} = 0.029 \pm 0.016 R_A$ (1σ , $n =$
30 50); CO_2/N_2 up to 3.7 – 57.8]. Crustal-scale active deformation driven by strike-slip faulting could
31 mobilize ^4He and CO_2 from the fault zone rocks, which subsequently accumulate in the
32 hydrothermal system. The Karakoram fault may have limited fluid connections to the mantle,
33 and if any, the accumulated crustal fluids would efficiently dilute the uprising mantle fluids. In
34 both cases, crustal deformation is evidently the first-order response to strike-slip faulting.

35

Plain Language Summary

37 Bubbling hot springs are common in fault zones along which Earth's lithosphere cracks.
38 Chemical and isotopic compositions of spring gases can offer key information on the subsurface
39 connectivity of the deep-rooting faults that is not easily visible. To assess whether the
40 Karakoram fault in western Tibetan Plateau is developing in the crust or extends into deeper
41 mantle, we studied the origin and transport of spring gases and found that the Karakoram fault is
42 overwhelmingly dominated by degassing of a crustal fluid reservoir that contains high amounts
43 of helium (He) and CO_2 . This could be attributed to He- CO_2 mobilization of deforming and
44 fracturing fault zone rocks at crustal depths, suggesting that the Karakoram fault is primarily
45 developing in the crust and may have limited fluid connections to the mantle.

46 **1. Introduction**

47 Continent-continent collision between India and Asia, as documented by the Himalayan-
48 Tibetan orogen, resulted in shortening and extrusion of the lithosphere over vast distances ([Ding](#)
49 [et al., 2022](#)). Whether the India-Asia collision is characterized by deformation confined to crustal
50 depths, or alternatively, reaching the underlying mantle lithosphere, holds the key for unraveling
51 the dynamics of orogenic plateau growth driven by the forces acting on the colliding continents
52 ([Copley et al., 2011](#); [Royden et al., 2008](#)). Strike-slip faults are likely to penetrate through brittle-
53 ductile transition zone and offset the Moho ([Bourne et al., 1998](#); [Sylvester, 1988](#)), thus providing
54 a window for gaining insights into the collision-driven deformation from mantle to crustal depths.
55 Therefore, the depth extent of strike-slip faults is a key parameter in modeling outward growth of
56 the Tibetan Plateau in response to India-Asia collision.

57 The right-lateral Karakoram fault (KKF) extends >1000 km from the Pamir to western
58 Himalayas (Figure [1a](#)), serving as an important plate boundary to accommodate shortening and
59 modulate eastward extrusion of the Tibetan Plateau ([Chevalier et al., 2015](#)). The depth extent of
60 the KKF penetration and deformation is still debated between kinematic models in favor of either
61 crustal- or lithospheric-scale strike-slip faulting ([Leech, 2008](#); [Searle & Phillips, 2007](#); [Van Buer](#)
62 [et al., 2015](#)). As the KKF exhibits geometrical segmentation (inset in Figure [1b](#)) and varies in
63 kinematics among different fault segments ([Robinson et al., 2015](#)), shear deformation may have
64 heterogeneity along its strike. Such along-strike deformation has been examined for the
65 geological past by field observations and evidence from metamorphism, magmatism,
66 geochronology, and slip rate reconstruction ([Chevalier, 2019](#); [Searle & Phillips, 2007](#); [Wallis et](#)
67 [al., 2013](#)). However, what remains challenging is that how underlying active deformation could
68 be constrained by modern observations at the surface. GPS-based geodetic measurements have

69 been used to establish strain partitioning patterns and active deformation of the KKF and
70 adjacent regions (Wright et al., 2004), but surface strain rates may be less informative for
71 inferring whether the deforming layer extends into the mantle or whether it ends within the crust
72 (Royden et al., 2008).

73 An alternative approach for constraining active deformation at depth is the geochemistry
74 of hydrothermal fluids (e.g., thermal spring gases and waters), which is sensitive to tectonic and
75 physical processes in the deep-rooting fault zones (Rosen et al., 2018). In particular, integrating
76 geochemical data with geophysical observations (Gao et al., 2016) could provide unique insights
77 into underlying structure and active deformation. Previous studies have identified mantle fluids
78 in thermal springs and suggested that the depth extent of the KKF could reach lithospheric
79 mantle (Bai et al., 2023; Hoke et al., 2000; Klemperer et al., 2013). Notably, only two out of
80 nineteen geothermal fields on and off the KKF show unequivocal mantle fluids (Klemperer et al.,
81 2013): Menshi [referred to as Tirthapuri in Hoke et al. (2000)] on the KKF, and Langjiu [referred
82 to as Shiquanhe in Hoke et al. (2000)] ~45 km off the KKF to the NE (Figure 1a; see details in
83 *Section 2.2*). Zooming out from Menshi and Langjiu, it becomes evident that the KKF is long
84 and has several segments. From a geochemical point of view, our understanding of hydrothermal
85 degassing remains limited to constrain segmental characteristics of active deformation beneath
86 the KKF.

87 In this study, we focus on the origin and transport of deeply-sourced volatiles (e.g., He
88 and CO₂) released by thermal springs on and off the southern KKF (Figure 1b; northern KKF is
89 almost inaccessible for political reasons), aiming to provide new insights into active deformation
90 driven by strike-slip faulting in western Tibetan Plateau. Our new He isotope data indicate that
91 the KKF is dominated by crustal degassing both on and off its southern segments. A crustal ⁴He-

92 and CO₂-rich fluid reservoir is identified in the subsurface hydrothermal systems, which could be
93 attributed to crustal-scale active deformation that liberates large amounts of ⁴He and CO₂ from
94 deforming and fracturing fault zone rocks. We further examined mantle-to-crust fluid
95 connections of the KKF and the dilution effects of crustal ⁴He-rich fluids based on regional
96 seismic data.

97

98 **2. Materials and Methods**

99 *2.1. Sample Distribution and Laboratory Analysis*

100 We adopted geometrical segmentation of the KKF (inset in Figure 1b; [Chevalier et al.,](#)
101 [2015](#)) to describe sample distribution. Seventeen free gas samples were collected from thermal
102 springs along the Gar and Menshi-Kailas segments, as well as the Langjiu geothermal field off
103 the KKF (Figure 1a). Due to the limits by transportation conditions and accessibility factors, we
104 were unable to collect samples from other fault segments. For example, the K2 segment (i.e.,
105 northern KKF; Figure 1b) and Bangong-Chaxikang segment are barely accessible due to their
106 closeness to the politically unstable Kashmir and China-India border. Chemical and isotopic
107 compositions (e.g., ³He/⁴He and δ¹³C-CO₂) of hydrothermal gases were analyzed as soon as
108 possible to avoid post-sampling air contamination. Details of field campaign, sampling
109 procedures, analytical methods, and geochemical data are given in Text S1 and Table S1 of the
110 Supporting Information [S1](#).

111 *2.2. Helium Isotope Systematics and Data Compilation*

112 Helium isotope ratio [³He/⁴He (R) reported relative to R_A, where R_A = air ³He/⁴He = 1.39
113 × 10⁻⁶] of modern hydrothermal fluids is a unique tracer for quantifying the mixing between
114 crustal and mantle fluids that possibly occurs in active fault zones ([Caracausi et al., 2022](#); [Sano](#)

115 & Fischer, 2013; Umeda & Ninomiya, 2009). The convective upper mantle, i.e., source of mid-
116 ocean ridge basalts (MORB), has an uniform $^3\text{He}/^4\text{He}$ ratio of $8 \pm 1 R_A$ (Graham, 2002), while
117 that of the sub-continental lithospheric mantle (SCLM) is lower ($6.1 \pm 2.1 R_A$; Day et al., 2015).
118 In contrast, the continental crust has accumulated large amounts of radiogenic ^4He due to U-Th
119 decay through time, yielding significantly low $^3\text{He}/^4\text{He}$ ratios such as $0.02 R_A$ (Andrews, 1985).
120 Variable amounts of atmospheric He could be detected in the sample due to recharge of air-
121 saturated water (ASW) into hydrothermal systems and post-sampling contamination. As such,
122 the measured $^3\text{He}/^4\text{He}$ must be corrected assuming that all ^{20}Ne in the sample is derived from
123 ASW (Craig et al., 1978).

124 A reference X value of ~ 10 , where $X = (\text{He}/\text{Ne})_{\text{sample}}/(\text{He}/\text{Ne})_{\text{air}} \times \beta_{\text{Ne}}/\beta_{\text{He}}$, was used to
125 rule out data showing significant air contamination (Klemperer et al., 2022; Zhang et al., 2021a).
126 Our He isotope data are in high quality with $<1\%$ ASW-derived He (Figure 2). In addition, He
127 isotope data in literature were compiled and classified into the following groups: On-KKF (K2),
128 On-KKF (Gar), On-KKF (Menshi-Kailas), Off-KKF, western Lhasa block, and western
129 Himalayas (Data Set S1 in Supporting Information S1). Among them, six low X-value (mostly
130 <10) samples from four geothermal fields (i.e., Menshi, Changlung, Duoguoqu, and Xiongbacun)
131 on the K2 and Menshi-Kailas segments were excluded from discussion. In particular, Changlung
132 (Klemperer et al., 2013) and Duoguoqu (Bai et al., 2023) were suggested to discharge mantle
133 fluids but were not considered in this study due to uncertain data quality (Figure 2). To assess
134 whether unequivocal mantle fluids are releasing at Changlung and Duoguoqu, new He isotope
135 measurements need to be conducted in future; but this possibility does not impact our discussion
136 and conclusion.

137 Spatially, most samples are distributed on and off the Gar and Menshi-Kailas segments,
138 and four samples from [Klemperer et al. \(2013, 2022\)](#) are ~40–60 km off the Bangong-Chaxikang
139 segment (Figure 1). In addition, considering the lack of detailed field work to confirm the
140 affinity of the Kailas-Thakkhola segment to the KKF ([Chevalier, 2019](#)), our newly acquired data,
141 along with the compiled literature data, would be suitable for constraining hydrothermal
142 degassing from the southern KKF, including the Bangong-Chaxikang, Gar, and Menshi-Kailas
143 segments.

144

145 **3. Results and Discussion**

146 *3.1. Regional $^3\text{He}/^4\text{He}$ Variability and Possible Temporal Changes*

147 There is a general consensus that any air-corrected $^3\text{He}/^4\text{He}$ ratio (R_C) higher than $0.1 R_A$
148 ($>1\%$ mantle He inputs assuming $8 R_A$ for the mantle and $0.02 R_A$ for the crust) is considered
149 unambiguous evidence for mantle degassing ([Crossey et al., 2009](#)), i.e., fluid connections to the
150 mantle. Conversely, those lower than $0.1 R_A$ represent crustal degassing. All our samples ($R_C =$
151 $0.015\text{--}0.042 R_A$; Table S1 in Supporting Information S1) plot in the canonical range of crustal
152 $^3\text{He}/^4\text{He}$ ($0.01\text{--}0.05 R_A$; [Ballentine et al., 2002](#)) and have $<0.5\%$ mantle He inputs (Figure 2).
153 This resembles crustal degassing in the adjacent western Himalayas and western Lhasa block
154 (Figure 2). Note that Samples ZGG04, ZGZ08, and ZZB09 ([Klemperer et al., 2022](#)) in the
155 western Lhasa block have $1.1\text{--}2.1\%$ mantle He inputs (Figure 3a) but are far away from the KKF
156 ($\sim 150\text{--}300$ km; Figure 1a). We do not expect any fluid connections between the KKF and these
157 distant thermal springs; and indeed, [Klemperer et al. \(2022\)](#) attributed the $\sim 1\text{--}2\%$ mantle He
158 inputs to the release of primordial ^3He from asthenospheric mantle wedge.

159 New He isotope data show that geothermal fields on the Gar and Menshi-Kailas
160 segments, as well as the Langjiu geothermal field off the KKF, are characterized by degassing of
161 crustal fluids (Figure 2 and Figure 3a). As mentioned in the Introduction, previous studies (Hoke
162 et al., 2000; Klemperer et al., 2013, 2022; Zhao et al., 2002) identified mantle He degassing at
163 Menshi and Langjiu (Figure 1). Notably, those samples with mantle He inputs (3.5–28% at
164 Menshi and 2.1–3.1% at Langjiu) were collected in the 1990s, while the post-2015 samples [i.e.,
165 2021 and 2022 at Menshi and Langjiu (this study); 2017 at Menshi and Langjiu (S. Klemperer,
166 personal communication); 2015 and 2019 at Langjiu (Sun et al., 2023)] collectively provide
167 unambiguous evidence for crustal degassing (Figure S1 in Supporting Information S1). Such
168 contrasting results from the same geothermal fields, although not strictly the same sample
169 locality, are intriguing and could be attributed to complex subsurface fluid pathways that are able
170 to cause vastly different dilutions of mantle volatiles by crustal fluids. For example, complex
171 gas-water-rock interaction (e.g., subsurface calcite precipitation; Chiodini et al., 2015) could
172 influence the connectivity and permeability of fluid pathways across short length-scales, and on
173 time-scales of only a few years one conduit may become calcified and another conduit may open.
174 This could increase the residence time of mantle fluids in the crust and thus lead to high
175 possibility of crustal He contamination. Further information on the origin of hydrothermal fluids
176 could contribute to our understanding of the controlling factors for He degassing from the KKF.

177 ***3.2. Identification of A Crustal ⁴He-Rich Fluid Reservoir***

178 Hydrothermal gases from the KKF are enriched in either CO₂ or N₂, or both of them
179 (Table S1 in Supporting Information S1). These major gases, together with water, serve as the
180 carrier for He migration through the crust (Hong et al., 2010; O'Nions & Oxburgh, 1988). When
181 arriving at the surface, the thermal spring gases are expected to contain variable amounts of

182 major and trace gases due to their solubility (S) difference in water (Barry et al., 2013). We find
183 that He contents vary significantly from several parts per million by volume (ppmv) to as high as
184 ~1.0–1.6 vol.% (Table S1 and Data Set S1 in Supporting Information S1). About half of the
185 geothermal fields (9 out of 17) on and off the KKF have average He content higher than
186 economic threshold value (~1000 ppmv; Chen et al., 2023) for He resource exploration. Unlike
187 the 1990s Menshi and Langjiu samples (Hoke et al., 2000; Klemperer et al., 2013), new
188 observations in this century show that the KKF is overwhelmingly dominated by crustal
189 degassing [$^3\text{He}/^4\text{He} = 0.029 \pm 0.016 R_A$ (1σ , $n = 50$)]. Taken together, it is reasonable to infer
190 that there is a crustal ^4He -rich fluid reservoir in the hydrothermal systems beneath the KKF
191 (Figure 3a).

192 Spatially, the crustal He degassing is generally focused in a ~30-km-wide zone along the
193 KKF, with He contents decreasing toward more distant regions in the NE and SW, respectively
194 (Figure S2 in Supporting Information S1), suggesting that the KKF is a primary conduit for the
195 uprising and degassing of crustal ^4He -rich fluids. Temporally, except for the 1990s Menshi and
196 Langjiu samples, mantle fluid inputs to the hydrothermal systems were not observed throughout
197 the KKF (Figure 3a). One possibility is that the uprising mantle fluids, if any, could be entirely
198 contaminated by the crustal ^4He -rich fluid reservoir as mentioned above. The impulsive nature of
199 crustal He degassing has been highlighted for tectonically active regions (Caracausi et al., 2022),
200 which is particularly affected by earthquake events or cycles (Buttitta et al., 2020). We compiled
201 54 earthquakes ($M = 3.2$ – 5.6 , average hypocentral depth = ~32 km, time interval = 1990–2022)
202 that occurred on the KKF and in adjacent areas ± 50 km off the KKF (Data Set S2 in Supporting
203 Information S1). A prominent peak in earthquake frequency between 2002 and 2004 is observed,
204 and those occurred since 2000 forms an earthquake cluster in the Menshi-Kailas segment (Figure

205 S3 in Supporting Information S1). Although the KKF may be seismically less active (e.g.,
206 number of recorded earthquakes is small; [Chevalier, 2019](#)) than many other strike-slip faults
207 such as the Xianshuihe fault ([Liu et al., 2023](#)), the increased earthquakes and their clustering in
208 the Menshi-Kailas segment could result in enhanced release of crustal He ([Buttitta et al., 2020](#);
209 [Caracausi et al., 2022](#)) and complex changes in subsurface structural conditions (e.g., the closure
210 and opening of fluid conduits), which may have made it difficult to detect mantle He inputs in
211 the post-2015 samples at Menshi and Langjiu.

212 Many continental strike-slip faults worldwide, such as the San Andreas fault ([Kennedy et](#)
213 [al., 1997](#); [Kulongoski et al., 2013](#)), the North Anatolia fault ([de Leeuw et al., 2010](#); [Güleç et al.,](#)
214 [2002](#)), and the Xianshuihe fault ([Liu et al., 2023](#); [Zhang et al., 2021b](#)), are characterized by
215 mantle ^3He degassing in long time series and thus plausible fluid connections to the mantle. In
216 this respect, the available data from the KKF are insufficient to assess mantle-to-crust fluid
217 connections and the possible impulsive nature of crustal degassing, which requires continuous
218 $^3\text{He}/^4\text{He}$ monitoring of thermal springs and further integration with seismic data analysis and
219 geophysical detections of the underlying structures.

220 ***3.3. Carbon Origins and Secondary Hydrothermal Processes***

221 Because CO_2 is a major carrier for He and mantle fluids are negligible in the He
222 inventory, carbon origins in hydrothermal systems are expected to be controlled by
223 decarbonation of crustal materials (rather than the mantle), including the reduced and oxidized
224 carbon species (Figure 3b; e.g., organic matter and carbonate rocks). Following separation from
225 the original reservoir, the transport of CO_2 -rich fluids to the surface is always accompanied by
226 secondary processes such as solubility-controlled gas-water-rock interaction, calcite precipitation,

227 and fluid addition from other sources (Buttitta et al., 2023; Randazzo et al., 2022; Ray et al.,
228 2009; Van Soest et al., 1998).

229 The positive correlation between CO_2/N_2 and $\text{CO}_2/{}^4\text{He}$ ratios indicates that N_2 -rich gases
230 (roughly differing from the CO_2 -rich gases by $\text{CO}_2/\text{N}_2 < 2-3$; Figure S4a in Supporting
231 Information S1) tend to have lower $\text{CO}_2/{}^4\text{He}$ ratios. Particularly, average He content (5961 ppmv)
232 of the N_2 -rich gases is ~10 times that of the CO_2 -rich gases (523 ppmv; Figure S4b in Supporting
233 Information S1). The preferential dissolution of CO_2 in groundwater could enrich the exsolved
234 gases with high amounts of less soluble species such as N_2 and noble gases (Rizzo et al., 2019).
235 Such selective gas dissolution in groundwater is plausible to explain the $\text{CO}_2/{}^4\text{He}$ decrease in the
236 He- and N_2 -rich gases (Figure 3c). Moreover, the sequestration of dissolved inorganic carbon as
237 carbonate minerals (e.g., calcite) could also lower $\text{CO}_2/{}^4\text{He}$ ratios of residual gas and fluid phases
238 (Barry et al., 2020; Ray et al., 2009), which simultaneously leads to $\delta^{13}\text{C}$ variations depending on
239 temperature and pH of the spring water (Gilfillan et al., 2009; Hilton et al., 1998). Modeling
240 results show that calcite precipitation probably occurred at temperatures of ~90–170 °C (Figure
241 3d), or within an expected pH of 6–8 (Gilfillan et al., 2009). Assuming a geothermal gradient of
242 30 °C km^{-1} for the western Tibet, carbonate minerals may start to precipitate at ~5–6 km depth,
243 consistent with groundwater circulation of the KKF (Wang et al., 2022). The possibility of
244 calcite precipitation is supported by travertine surrounding spring mouths and calcite veins in
245 exhumed fault rocks (Wallis et al., 2013). In contrast, the increasing $\text{CO}_2/{}^4\text{He}$ with decreasing He
246 may result from hydrothermal degassing (Figure 3c), which preferentially retains CO_2 over He in
247 the residual fluid phase (i.e., $S_{\text{He}} \ll S_{\text{CO}_2}$ in aqueous fluids; Barry et al., 2014). Furthermore, CO_2
248 addition into the uprising hydrothermal fluids is also likely because a mixture of crustal reduced

249 and oxidized carbon could provide CO₂-rich fluids for mixing with those derived from the crustal
250 ⁴He-rich fluid reservoir (Figure 3d).

251 ***3.4. He-CO₂ Mobilization Related to Crustal-Scale Active Deformation***

252 Continental strike-slip faults are important conduits for the outgassing of deeply-sourced
253 volatiles such as He and CO₂ (Kim et al., 2020; Kulongoski et al., 2013; Xu et al., 2022; Zhang
254 et al., 2021b). A crustal ⁴He- and CO₂-rich fluid reservoir is proposed to sustain the prevailing
255 crustal degassing through the KKF (Figure 4). The formation of such ⁴He- and CO₂-rich fluid
256 reservoir depends on (i) liberation of He and CO₂ from variable sources by physical and
257 chemical processes, and (ii) their accumulation in the fluid reservoir as dissolved and gaseous
258 phases (Ballentine et al., 2002). Considering geological and structural features of the KKF, we
259 suggest that the mechanism that could mobilize He and CO₂ from crustal rocks is closely related
260 to active deformation driven by the Karakoram strike-slip faulting (Figure 4).

261 Strike-slip faults could offset the brittle upper crust and yield at depth to broadly
262 distributed shearing beneath the brittle-ductile transition zone (Figure 4). For the shear zone
263 rocks, dilatancy-related microscale fracturation could enhance the release of crustal ⁴He into pore
264 fluids (Caracausi et al., 2022). Moreover, deformation-enhanced fault permeability could
265 facilitate fluid infiltration into the carbon-bearing rocks, which thus increases the efficiency of
266 metamorphic decarbonation reactions (Stewart et al., 2019). Therefore, the deforming and
267 fracturing rocks in the ductile shear zone could release large amounts of crustal He and CO₂,
268 which subsequently migrate through the highly fractured fault zones into the hydrothermal
269 system and accumulate over time to form a ⁴He- and CO₂-rich fluid reservoir. At shallower
270 depths, water-rock interaction and mixing with shallow fluids (e.g., meteoric water infiltrating
271 sediments; Buttitta et al., 2023) could also contribute to the He-CO₂ inventory (Figure 4).

272 Overall, our model based on geochemical evidence agrees well with geological and geophysical
273 studies that suggest crustal-level localization and thus crustal-scale deformation of the KKF
274 (Craig et al., 2012; Gao et al., 2016; Searle & Phillips, 2007; Van Buer et al., 2015; Wang &
275 Klemperer, 2021).

276

277 **4. Conclusions**

278 This study presents an attempt to locate the penetration depth and active deformation of
279 continental strike-slip faults based on chemical and isotopic compositions of hydrothermal gases.
280 Our main finding is the crustal ^4He - and CO_2 -rich fluid reservoir in the subsurface hydrothermal
281 system, which sustains the prevailing crustal degassing from the southern KKF. The failure of
282 the post-2015 measurements in identifying mantle fluids at Menshi and Langjiu may result from
283 (i) complex subsurface fluid conduits that could be changed by hydrothermal processes (e.g.,
284 calcite precipitation) and regional seismicity, and (ii) the earthquake cluster in the Menshi-Kailas
285 segment since 2000. Specifically, the former increases the possibility of mantle fluids being
286 diluted by the crustal ^4He - and CO_2 -rich fluids, while the latter enhances the liberation of crustal
287 ^4He and CO_2 from deforming and fracturing fault zone rocks. Although more data are required to
288 evaluate the mantle-to-crust fluid connections and possible impulsive nature of crustal degassing,
289 crustal-scale active deformation is evidently a fundamental response to strike-slip faulting of the
290 southern KKF. Our results provide new geochemical evidence for the penetration depth and
291 active deformation of the KKF, which would be enlightening for interpreting active formation
292 driven by continental strike-slip faults in global orogenic belts.

293

294 **Acknowledgments**

295 This work was supported by National Natural Science Foundation of China (NSFC)
296 (41930642) and National Key Research and Development Program of China
297 (2020YFA0607700). MZ acknowledges an NSFC grant 42072327. We are grateful to Prof.
298 Simon L. Klemperer and an anonymous reviewer for their constructive and insightful comments
299 that have significantly improved the quality of this manuscript.

300

301 **Open Research**

302 Data supporting the findings of this study are available at Zhang (2023)
303 <https://doi.org/10.5281/zenodo.10297762>.

304

305 **References**

306 Andrews, J. N. (1985). The isotopic composition of radiogenic helium and its use to study
307 groundwater movement in confined aquifers. *Chemical Geology*, 49(1), 339–351.

308 [https://doi.org/10.1016/0009-2541\(85\)90166-4](https://doi.org/10.1016/0009-2541(85)90166-4)

309 Bai, Y., Shi, Z., Zhou, X., Wu, C., Wang, G., He, M., et al. (2023). Gas geochemical evidence
310 for the India-Asia lithospheric transition boundary near the Karakorum fault in western

311 Tibet. *Chemical Geology*, 639, 121728. <https://doi.org/10.1016/j.chemgeo.2023.121728>

312 Ballentine, C. J., Burgess, R., & Marty, B. (2002). Tracing fluid origin, transport and interaction
313 in the crust. *Reviews in Mineralogy and Geochemistry*, 47(1), 539–614.

314 <https://doi.org/10.2138/rmg.2002.47.13>

315 Barry, P. H., Hilton, D. R., Füre, E., Halldórsson, S. A., & Grönvold, K. (2014). Carbon isotope
316 and abundance systematics of Icelandic geothermal gases, fluids and subglacial basalts

- 317 with implications for mantle plume-related CO₂ fluxes. *Geochimica et Cosmochimica*
318 *Acta*, 134, 74–99. <http://doi.org/10.1016/j.gca.2014.02.038>
- 319 Barry, P. H., Hilton, D. R., Fischer, T. P., de Moor, J. M., Mangasini, F., & Ramirez, C. (2013).
320 Helium and carbon isotope systematics of cold “mazuku” CO₂ vents and hydrothermal
321 gases and fluids from Rungwe Volcanic Province, southern Tanzania. *Chemical*
322 *Geology*, 339, 141–156. <http://doi.org/10.1016/j.chemgeo.2012.07.003>
- 323 Barry, P. H., Negrete-Aranda, R., Spelz, R. M., Seltzer, A. M., Bekaert, D. V., Virrueta, C., &
324 Kulongoski, J. T. (2020). Volatile sources, sinks and pathways: A helium-carbon isotope
325 study of Baja California fluids and gases. *Chemical Geology*, 550, 119722.
326 <https://doi.org/10.1016/j.chemgeo.2020.119722>
- 327 Bourne, S. J., England, P. C., & Parsons, B. (1998). The motion of crustal blocks driven by flow
328 of the lower lithosphere and implications for slip rates of continental strike-slip faults.
329 *Nature*, 391(6668), 655–659. <https://doi.org/10.1038/35556>
- 330 Buttitta, D., Caracausi, A., Chiaraluce, L., Favara, R., Gasparo Morticelli, M., & Sulli, A.
331 (2020). Continental degassing of helium in an active tectonic setting (northern Italy): the
332 role of seismicity. *Scientific Reports*, 10(1), 162. [https://doi.org/10.1038/s41598-019-](https://doi.org/10.1038/s41598-019-55678-7)
333 [55678-7](https://doi.org/10.1038/s41598-019-55678-7)
- 334 Buttitta, D., Capasso, G., Paternoster, M., Barberio, M. D., Gori, F., Petitta, M., et al. (2023).
335 Regulation of deep carbon degassing by gas-rock-water interactions in a seismic region
336 of Southern Italy. *Science of the Total Environment*, 897, 165367.
337 <https://doi.org/10.1016/j.scitotenv.2023.165367>
- 338 Caracausi, A., Buttitta, D., Picozzi, M., Paternoster, M., & Stabile, T. A. (2022). Earthquakes
339 control the impulsive nature of crustal helium degassing to the atmosphere.

- 340 *Communications Earth & Environment*, 3(1), 224. [https://doi.org/10.1038/s43247-022-](https://doi.org/10.1038/s43247-022-00549-9)
341 [00549-9](https://doi.org/10.1038/s43247-022-00549-9)
- 342 Chen, B., Liu, Y., Fang, L., Xu, S., Stuart, F. M., & Liu, C. (2023). A review of noble gas
343 geochemistry in natural gas from sedimentary basins in China. *Journal of Asian Earth*
344 *Sciences*, 246, 105578. <https://doi.org/10.1016/j.jseaes.2023.105578>
- 345 Chevalier, M.-L. (2019). Active tectonics along the Karakorum fault, western Tibetan Plateau:
346 A review. *Acta Geoscientica Sinica*, 40(1), 37–54.
347 <https://doi.org/10.3975/cagsb.2018.101601>
- 348 Chevalier, M.-L., Van der Woerd, J., Tapponnier, P., Li, H., Ryerson, F. J., & Finkel, R. C.
349 (2015). Late Quaternary slip-rate along the central Bangong-Chaxikang segment of the
350 Karakorum fault, western Tibet. *Geological Society of America Bulletin*, 128(1–2), 284–
351 314. <https://doi.org/10.1130/B31269.1>
- 352 Chiodini, G., Pappalardo, L., Aiuppa, A., & Caliro, S. (2015). The geological CO₂ degassing
353 history of a long-lived caldera. *Geology*, 43(9), 767–770.
354 <https://doi.org/10.1130/g36905.1>
- 355 Copley, A., Avouac, J.-P., & Wernicke, B. P. (2011). Evidence for mechanical coupling and
356 strong Indian lower crust beneath southern Tibet. *Nature*, 472(7341), 79–81.
357 <http://doi.org/10.1038/nature09926>
- 358 Craig, H., Lupton, J., & Horibe, Y. (1978). A mantle helium component in circum-Pacific
359 volcanic gases: Hakone, the Marianas, and Mt. Lassen, in *Advances in Earth and*
360 *Planetary Science Terrestrial Rare Gases*, edited by E. C. Alexander & M. Ozima, pp.
361 3-16, Academic publication, Japan

- 362 Craig, T. J., Copley, A., & Jackson, J. (2012). Thermal and tectonic consequences of India
363 underthrusting Tibet. *Earth and Planetary Science Letters*, 353–354, 231–239.
364 <https://doi.org/10.1016/j.epsl.2012.07.010>
- 365 Crossey, L. J., Karlstrom, K. E., Springer, A. E., Newell, D., Hilton, D. R., & Fischer, T. (2009).
366 Degassing of mantle-derived CO₂ and He from springs in the southern Colorado Plateau
367 region—Neotectonic connections and implications for groundwater systems. *Geological*
368 *Society of America Bulletin*, 121(7–8), 1034–1053. <https://doi.org/10.1130/b26394.1>
- 369 Day, J. M. D., Barry, P. H., Hilton, D. R., Burgess, R., Pearson, D. G., & Taylor, L. A. (2015).
370 The helium flux from the continents and ubiquity of low-³He/⁴He recycled crust and
371 lithosphere. *Geochimica et Cosmochimica Acta*, 153, 116–133.
372 <https://doi.org/10.1016/j.gca.2015.01.008>
- 373 de Leeuw, G. A. M., Hilton, D. R., Güleç, N., & Mutlu, H. (2010). Regional and temporal
374 variations in CO₂/³He, ³He/⁴He and δ¹³C along the North Anatolian Fault Zone, Turkey.
375 *Applied Geochemistry*, 25(4), 524–539.
376 <https://doi.org/10.1016/j.apgeochem.2010.01.010>
- 377 Ding, L., Kapp, P., Cai, F., Garzzone, C. N., Xiong, Z., Wang, H., & Wang, C. (2022). Timing
378 and mechanisms of Tibetan Plateau uplift. *Nature Reviews Earth & Environment*, 3,
379 652–667. <https://doi.org/10.1038/s43017-022-00318-4>
- 380 Gao, R., Lu, Z., Klemperer, S. L., Wang, H., Dong, S., Li, W., & Li, H. (2016). Crustal-scale
381 duplexing beneath the Yarlung Zangbo suture in the western Himalaya. *Nature*
382 *Geoscience*, 9, 555–560. <http://doi.org/10.1038/ngeo2730>

- 383 Gilfillan, S. M. V., Lollar, B. S., Holland, G., Blagburn, D., Stevens, S., Schoell, M., et al.
384 (2009). Solubility trapping in formation water as dominant CO₂ sink in natural gas fields.
385 *Nature*, 458(7238), 614–618. <https://doi.org/10.1038/nature07852>
- 386 Graham, D. W. (2002). Noble gas isotope geochemistry of mid-ocean ridge and ocean island
387 basalts: Characterization of mantle source reservoirs. *Reviews in Mineralogy and*
388 *Geochemistry*, 47, 247–319. <https://doi.org/10.2138/rmg.2002.47.8>
- 389 Güleç, N., Hilton, D. R., & Mutlu, H. (2002). Helium isotope variations in Turkey: relationship
390 to tectonics, volcanism and recent seismic activities. *Chemical Geology*, 187(1–2), 129–
391 142. [https://doi.org/10.1016/s0009-2541\(02\)00015-3](https://doi.org/10.1016/s0009-2541(02)00015-3)
- 392 Hilton, D. R., McMurtry, G. M., & Goff, F. (1998). Large variations in vent fluid CO₂³He ratios
393 signal rapid changes in magma chemistry at Loihi seamount, Hawaii. *Nature*, 396, 359–
394 362. <http://doi.org/10.1038/24603>
- 395 Hoke, L., Lamb, S., Hilton, D. R., & Poreda, R. J. (2000). Southern limit of mantle-derived
396 geothermal helium emissions in Tibet: Implications for lithospheric structure. *Earth and*
397 *Planetary Science Letters*, 180(3–4), 297–308. [https://doi.org/10.1016/S0012-](https://doi.org/10.1016/S0012-821X(00)00174-6)
398 [821X\(00\)00174-6](https://doi.org/10.1016/S0012-821X(00)00174-6)
- 399 Hong, W.-L., Yang, T. F., Walia, V., Lin, S.-J., Fu, C.-C., Chen, Y.-G., et al. (2010). Nitrogen
400 as the carrier gas for helium emission along an active fault in NW Taiwan. *Applied*
401 *Geochemistry*, 25(4), 593–601. <https://doi.org/10.1016/j.apgeochem.2010.01.016>
- 402 Kennedy, B. M., Kharaka, Y. K., Evans, W. C., Ellwood, A., DePaolo, D. J., Thordsen, J., et al.
403 (1997). Mantle fluids in the San Andreas fault system, California. *Science*, 278(5341),
404 1278–1281. <http://doi.org/10.1126/science.278.5341.1278>

- 405 Kim, H., Lee, H., Lee, J., Lee, H. A., Woo, N. C., Lee, Y.-S., et al. (2020). Mantle-derived
406 helium emission near the Pohang EGS Site, South Korea: Implications for active fault
407 distribution. *Geofluids*, 2020, 2359740. <https://doi.org/10.1155/2020/2359740>
- 408 Klemperer, S. L., Kennedy, B. M., Sastry, S. R., Makovsky, Y., Harinarayana, T., & Leech, M.
409 L. (2013). Mantle fluids in the Karakoram fault: Helium isotope evidence. *Earth and*
410 *Planetary Science Letters*, 366, 59–70. <https://doi.org/10.1016/j.epsl.2013.01.013>
- 411 Klemperer, S. L., Zhao, P., Whyte, C. J., Darrah, T. H., Crossey, L. J., Karlstrom, K. E., et al.
412 (2022). Limited underthrusting of India below Tibet: $^3\text{He}/^4\text{He}$ analysis of thermal springs
413 locates the mantle suture in continental collision. *Proceedings of the National Academy*
414 *of Sciences*, 119(12), e2113877119. <https://doi.org/10.1073/pnas.2113877119>
- 415 Kulongoski, J. T., Hilton, D. R., Barry, P. H., Esser, B. K., Hillemonds, D., & Belitz, K. (2013).
416 Volatile fluxes through the Big Bend section of the San Andreas Fault, California:
417 Helium and carbon-dioxide systematics. *Chemical Geology*, 339, 92–102.
418 <https://doi.org/10.1016/j.chemgeo.2012.09.007>
- 419 Leech, M. L. (2008). Does the Karakoram fault interrupt mid-crustal channel flow in the
420 western Himalaya? *Earth and Planetary Science Letters*, 276(3), 314–322.
421 <https://doi.org/10.1016/j.epsl.2008.10.006>
- 422 Liu, W., Zhang, M., Chen, B., Liu, Y., Cao, C., Xu, W., et al. (2023). Hydrothermal He and CO₂
423 degassing from a Y-shaped active fault system in eastern Tibetan Plateau with
424 implications for seismogenic processes. *Journal of Hydrology*, 620, 129482.
425 <https://doi.org/10.1016/j.jhydrol.2023.129482>

- 426 O'Nions, R. K., & Oxburgh, E. R. (1988). Helium, volatile fluxes and the development of
427 continental crust. *Earth and Planetary Science Letters*, *90*, 331–347.
428 [https://doi.org/10.1016/0012-821X\(88\)90134-3](https://doi.org/10.1016/0012-821X(88)90134-3)
- 429 Randazzo, P., Caracausi, A., Aiuppa, A., Cardellini, C., Chiodini, G., Apollaro, C., et al. (2022).
430 Active degassing of crustal CO₂ in areas of tectonic collision: A case study from the
431 Pollino and Calabria sectors (Southern Italy). *Frontiers in Earth Science*, *10*, 946707.
432 <https://doi.org/10.3389/feart.2022.946707>
- 433 Ray, M. C., Hilton, D. R., Muñoz, J., Fischer, T. P., & Shaw, A. M. (2009). The effects of
434 volatile recycling, degassing and crustal contamination on the helium and carbon
435 geochemistry of hydrothermal fluids from the Southern Volcanic Zone of Chile.
436 *Chemical Geology*, *266*(1–2), 38–49. <https://doi.org/10.1016/j.chemgeo.2008.12.026>
- 437 Rizzo, A. L., Caracausi, A., Chavagnac, V., Nomikou, P., Polymenakou, P. N., Mandalakis, M.,
438 et al. (2019). Geochemistry of CO₂-Rich Gases Venting From Submarine Volcanism:
439 The Case of Kolumbo (Hellenic Volcanic Arc, Greece). *Frontiers in Earth Science*, *7*.
440 <https://doi.org/10.3389/feart.2019.00060>
- 441 Robinson, A. C., Owen, L. A., Chen, J., Schoenbohm, L. M., Hedrick, K. A., Blisniuk, K., et al.
442 (2015). No late Quaternary strike-slip motion along the northern Karakoram fault. *Earth
443 and Planetary Science Letters*, *409*, 290–298. <https://doi.org/10.1016/j.epsl.2014.11.011>
- 444 Rosen, M. R., Binda, G., Archer, C., Pozzi, A., Michetti, A. M., & Noble, P. J. (2018).
445 Mechanisms of earthquake-induced chemical and fluid transport to carbonate
446 groundwater springs after earthquakes. *Water Resources Research*, *54*(8), 5225–5244.
447 <https://doi.org/10.1029/2017WR022097>

- 448 Royden, L. H., Burchfiel, B. C., & van der Hilst, R. D. (2008). The geological evolution of the
449 Tibetan Plateau. *Science*, *321*(5892), 1054–1058.
450 <https://doi.org/10.1126/science.1155371>
- 451 Sano, Y., & Fischer, T. P. (2013). The analysis and interpretation of noble gases in modern
452 hydrothermal systems, in *The Noble Gases as Geochemical Tracers*, edited by P.
453 Burnard, pp. 249–317, Springer, Berlin Heidelberg. [http://doi.org/10.1007/978-3-642-](http://doi.org/10.1007/978-3-642-28836-4_10)
454 [28836-4_10](http://doi.org/10.1007/978-3-642-28836-4_10)
- 455 Searle, M. P., & Phillips, R. J. (2007). Relationships between right-lateral shear along the
456 Karakoram fault and metamorphism, magmatism, exhumation and uplift: evidence from
457 the K2–Gasherbrum–Pangong ranges, north Pakistan and Ladakh. *Journal of the*
458 *Geological Society*, *164*(2), 439–450. <https://doi.org/10.1144/0016-76492006-072>
- 459 Stewart, E. M., Ague, J. J., Ferry, J. M., Schiffries, C. M., Tao, R.-B., Isson, T. T., & Planavsky,
460 N. J. (2019). Carbonation and decarbonation reactions: Implications for planetary
461 habitability. *American Mineralogist*, *104*(10), 1369–1380. [https://doi.org/10.2138/am-](https://doi.org/10.2138/am-2019-6884)
462 [2019-6884](https://doi.org/10.2138/am-2019-6884)
- 463 Sun, Y., Guo, Z., Fortin, D., Zhao, W., Cheng, Z., Li, J., & Zhang, Y. (2023). Diffuse emission
464 of CO₂ from the Langjiu Geothermal Field, Western Tibet. *Journal of Geochemical*
465 *Exploration*, *249*, 107219. <https://doi.org/10.1016/j.gexplo.2023.107219>
- 466 Sylvester, A. G. (1988). Strike-slip faults. *Geological Society of America Bulletin*, *100*(11),
467 1666–1703. [https://doi.org/10.1130/0016-7606\(1988\)100](https://doi.org/10.1130/0016-7606(1988)100<1666:SSF>2.3.CO;2)<1666:SSF>2.3.CO;2
- 468 Umeda, K., & Ninomiya, A. (2009). Helium isotopes as a tool for detecting concealed active
469 faults. *Geochemistry, Geophysics, Geosystems*, *10*(8), Q08010.
470 <https://doi.org/10.1029/2009GC002501>

- 471 Van Buer, N. J., Jagoutz, O., Upadhyay, R., & Guillong, M. (2015). Mid-crustal detachment
472 beneath western Tibet exhumed where conjugate Karakoram and Longmu–Gozha Co
473 faults intersect. *Earth and Planetary Science Letters*, *413*, 144–157.
474 <https://doi.org/10.1016/j.epsl.2014.12.053>
- 475 Van Soest, M. C., Hilton, D. R., & Kreulen, R. (1998). Tracing crustal and slab contributions to
476 arc magmatism in the Lesser Antilles island arc using helium and carbon relationships in
477 geothermal fluids. *Geochimica et Cosmochimica Acta*, *62*(19–20), 3323–3335.
478 [https://doi.org/10.1016/S0016-7037\(98\)00241-5](https://doi.org/10.1016/S0016-7037(98)00241-5)
- 479 Wallis, D., Phillips, R. J., & Lloyd, G. E. (2013). Fault weakening across the frictional-viscous
480 transition zone, Karakoram Fault Zone, NW Himalaya. *Tectonics*, *32*(5), 1227–1246.
481 <https://doi.org/10.1002/tect.20076>
- 482 Wang, J., Zhou, X., He, M., Li, J., Dong, J., Tian, J., et al. (2022). Hydrogeochemical origin and
483 circulation of spring waters along the Karakorum fault, Western Tibetan Plateau:
484 Implications for interaction between hydrosphere and lithosphere. *Frontiers in Earth
485 Science*, *10*, 1021550. <https://doi.org/10.3389/feart.2022.1021550>
- 486 Wang, S., & Klemperer, S. L. (2021). Love-wave normal modes discriminate between upper-
487 mantle and crustal earthquakes: Simulation and demonstration in Tibet. *Earth and
488 Planetary Science Letters*, *571*, 117089. <https://doi.org/10.1016/j.epsl.2021.117089>
- 489 Wright, T. J., Parsons, B., England, P. C., & Fielding, E. J. (2004). InSAR observations of low
490 slip rates on the major faults of western Tibet. *Science*, *305*(5681), 236–239.
491 <https://doi.org/10.1126/science.1096388>
- 492 Xu, S., Guan, L., Zhang, M., Zhong, J., Liu, W., Xie, X. g., et al. (2022). Degassing of deep-
493 sourced CO₂ from Xianshuihe-Anninghe fault zones in the eastern Tibetan Plateau.

494 *Science China Earth Sciences*, 65(1), 139–155. [https://doi.org/10.1007/s11430-021-](https://doi.org/10.1007/s11430-021-9810-x)
495 [9810-x](https://doi.org/10.1007/s11430-021-9810-x)

496 Zhang, M. (2023). mzhangrocks/KarakoramFault: Data files for hydrothermal degassing from
497 the Karakoram fault [Data set]. Zenodo. <https://doi.org/10.5281/zenodo.10297762>

498 Zhang, M., Xu, S., Zhou, X., Caracausi, A., Sano, Y., Guo, Z., et al. (2021a). Deciphering a
499 mantle degassing transect related with India-Asia continental convergence from the
500 perspective of volatile origin and outgassing. *Geochimica et Cosmochimica Acta*, 310,
501 61–78. <https://doi.org/10.1016/j.gca.2021.07.010>

502 Zhang, M., Guo, Z., Xu, S., Barry, P. H., Sano, Y., Zhang, L., et al. (2021b). Linking deeply-
503 sourced volatile emissions to plateau growth dynamics in southeastern Tibetan Plateau.
504 *Nature Communications*, 12(1), 4157. <https://doi.org/10.1038/s41467-021-24415-y>

505 Zhao, P., Xie, E., Dor, J., Jin, J., Hu, X., Du, S., & Yao, Z. (2002). Geochemical characteristics
506 of geothermal gases and their geological implications in Tibet. *Acta Petrologica Sinica*,
507 18(4), 539–550. (in Chinese with English abstract).

508

509 **Figure Caption**

510

511 **Figure 1.** (a) Map showing geo-tectonic framework and sample locality. Bold italic letters M and
512 L refer to Menshi and Langjiu, respectively. (b) Enlarged map of the southern Karakoram fault.
513 Insert of fault segmentation is after [Chevalier et al. \(2015\)](#). The compiled earthquake events
514 (Data Set S2 in Supporting Information S1) are from USGS Earthquake Catalog.

515

516 **Figure 2.** Plot of $^3\text{He}/^4\text{He}$ (R_M/R_A) versus X value. Filled and open symbols represent data in this
517 study and literature, respectively. Air-saturated water (ASW; $^3\text{He}/^4\text{He} = 0.985 R_A$, $^4\text{He}/^{20}\text{Ne} =$

518 0.26) is from [Klemperer et al. \(2022\)](#). Mantle end-member refers to a combination of depleted
519 MORB-sourced mantle ($8 \pm 1 R_A$; [Graham, 2002](#)) and SCLM ($6.1 \pm 2.1 R_A$; [Day et al., 2015](#)).
520 Crust-mantle mixtures with variable mantle proportions, calculated from mixing between
521 MORB-type mantle ($8 R_A$) and crust ($0.02 R_A$), are shown for comparison. $^4\text{He}/^{20}\text{Ne}$ ratio of
522 crust, mantle, and crust-mantle mixtures is assumed to be 3500. Changlung (CL) and Duoguoqu
523 (DGQ) are shown for comparison with the 1990s Menshi and Langjiu samples. The horizontal
524 scale bar represents proportions of ASW-derived He in uncorrected $^3\text{He}/^4\text{He}$ values.

525

526

527 **Figure 3.** Plots of He-CO₂ systematics. (a) $^3\text{He}/^4\text{He}$ (R_C/R_A) versus $1/\text{He}$. (b) $^3\text{He}/^4\text{He}$ (R_C/R_A)
528 versus $\delta^{13}\text{C-CO}_2$ (‰). (c) $\text{CO}_2/^4\text{He}$ versus $1/\text{He}$. (d) $\text{CO}_2/^4\text{He}$ versus $\delta^{13}\text{C-CO}_2$ (‰). Data source
529 and symbols are as in [Figure 2](#). The initially exsolved gases from crustal fluid reservoir are
530 defined according to geochemical tendency of samples. Reference values of end-member
531 parameters are given in [Table S2](#) in [Supporting Information S1](#). Note that in some cases the
532 $\delta^{13}\text{C-CO}_2$ value of mantle fluids could be comparable with that of the mixture between crustal
533 reduced and oxidized carbon; however, crustal ^4He -rich fluids are expected to have lower
534 $\text{CO}_2/^4\text{He}$ than mantle fluids due to excessed ^4He relative to CO_2 . Model of calcite precipitation
535 (CP) is after [Barry et al. \(2020\)](#).

536

537 **Figure 4.** Cartoon showing crustal-scale active deformation and related hydrothermal degassing.
538 Groundwater circulation depth is after [Wang et al. \(2022\)](#) and the brittle-ductile transition zone is
539 assumed to be at ~ 30 km depth for western Tibet.

Figure 1.

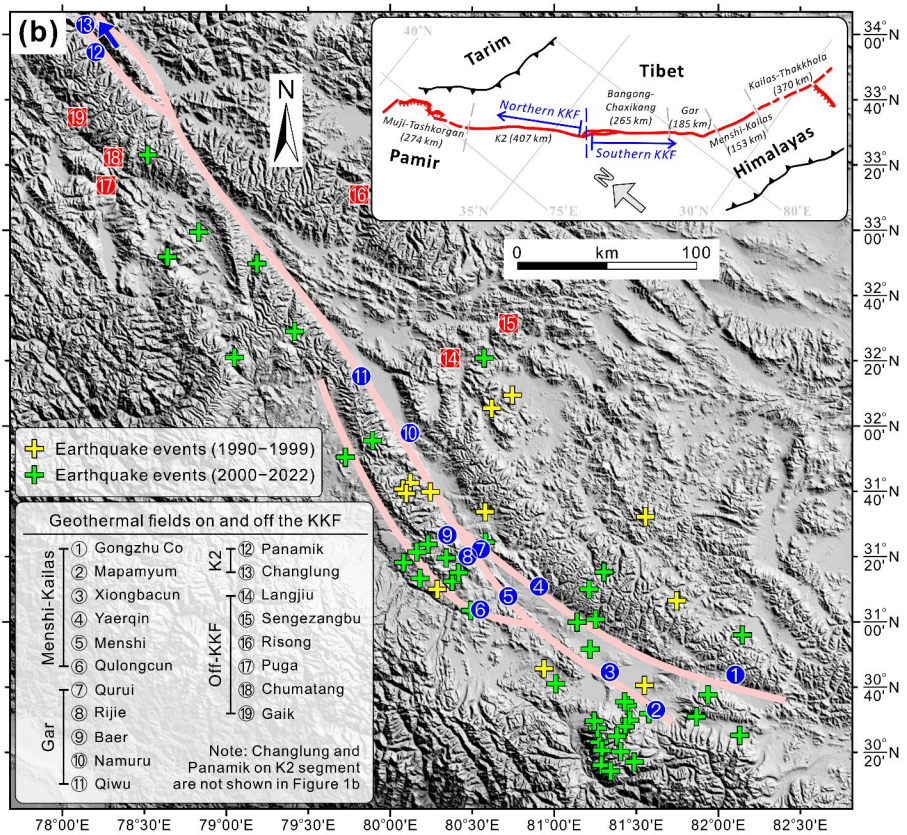
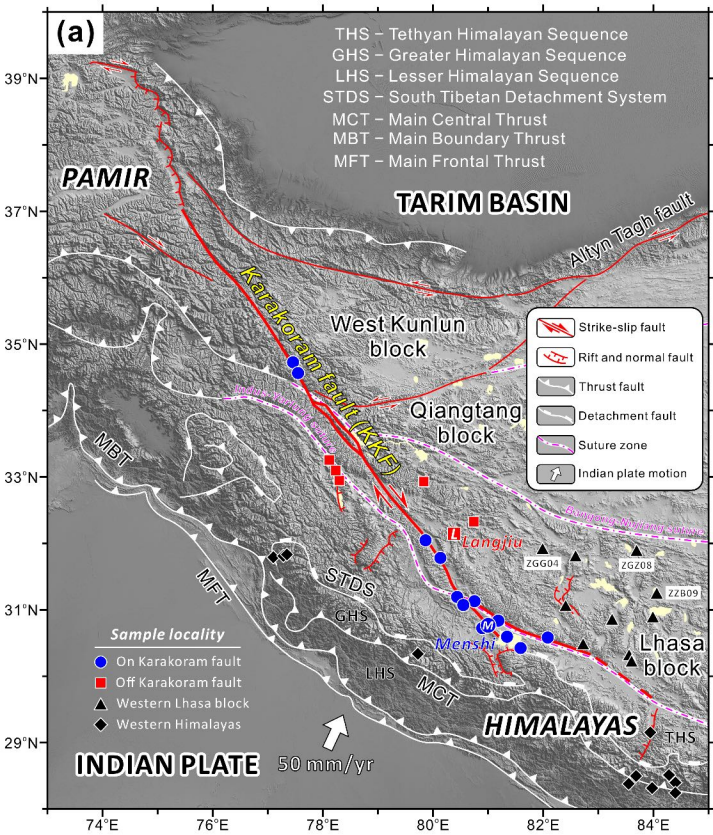


Figure 2.

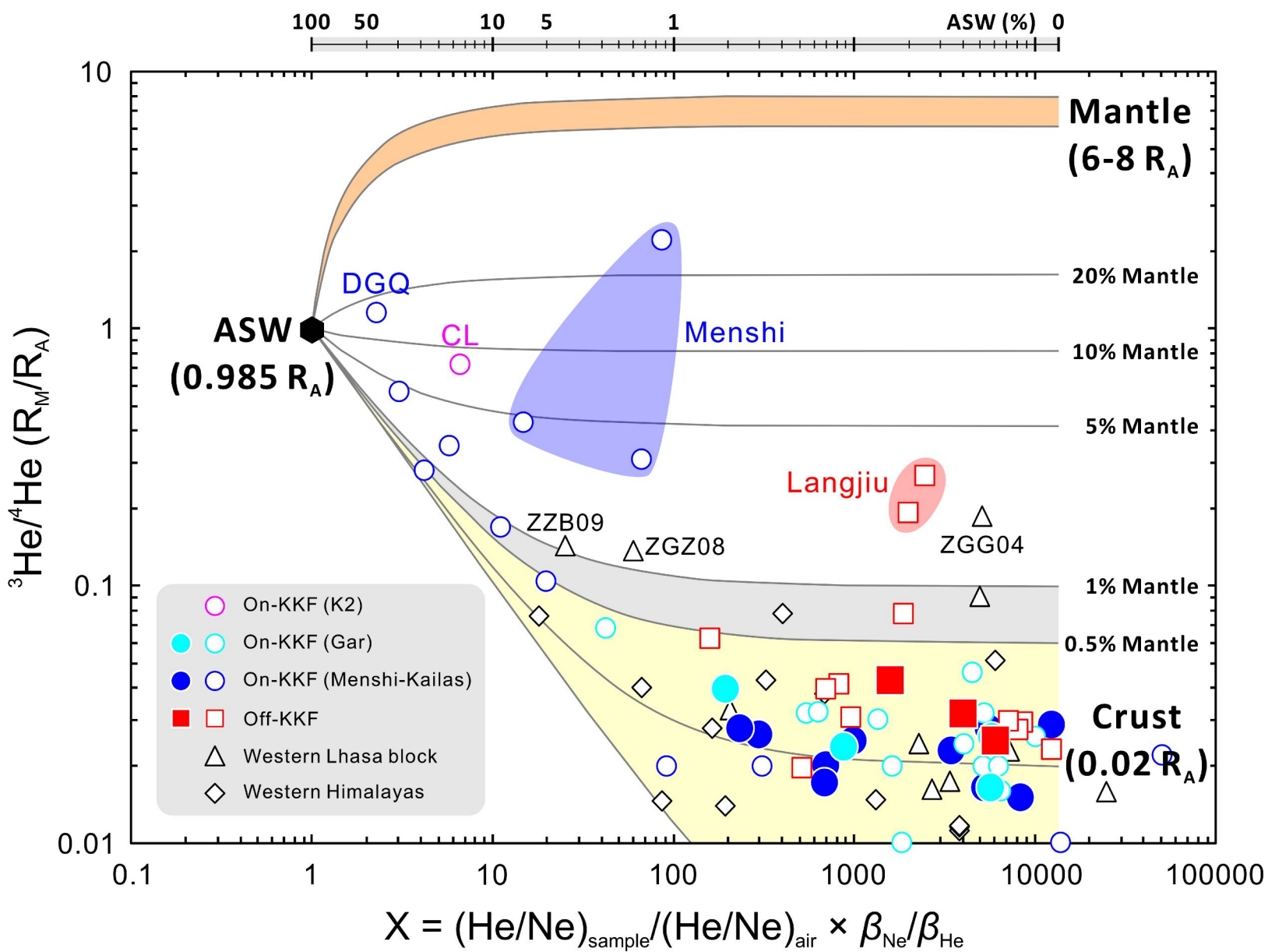


Figure 3.

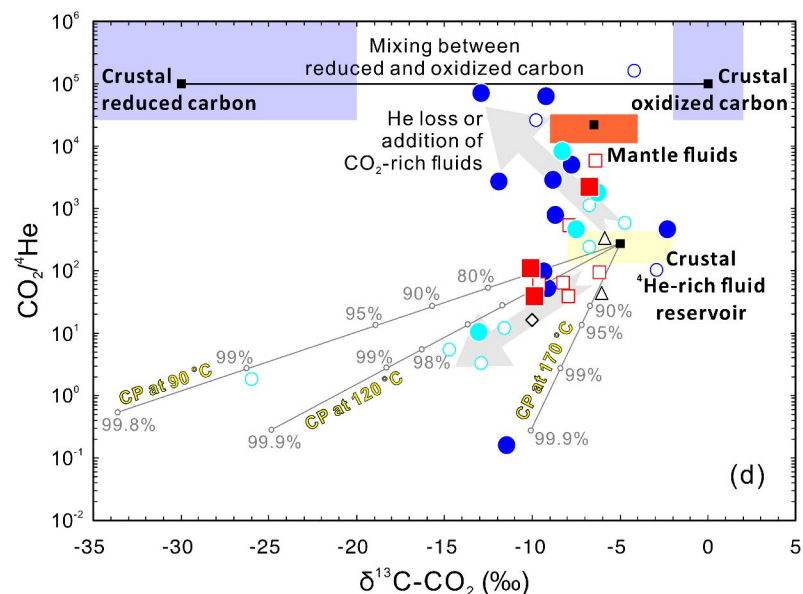
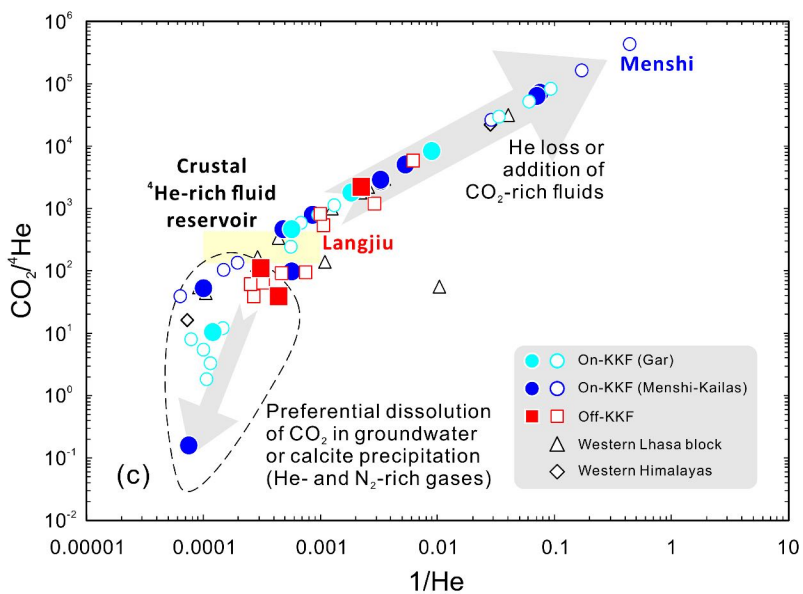
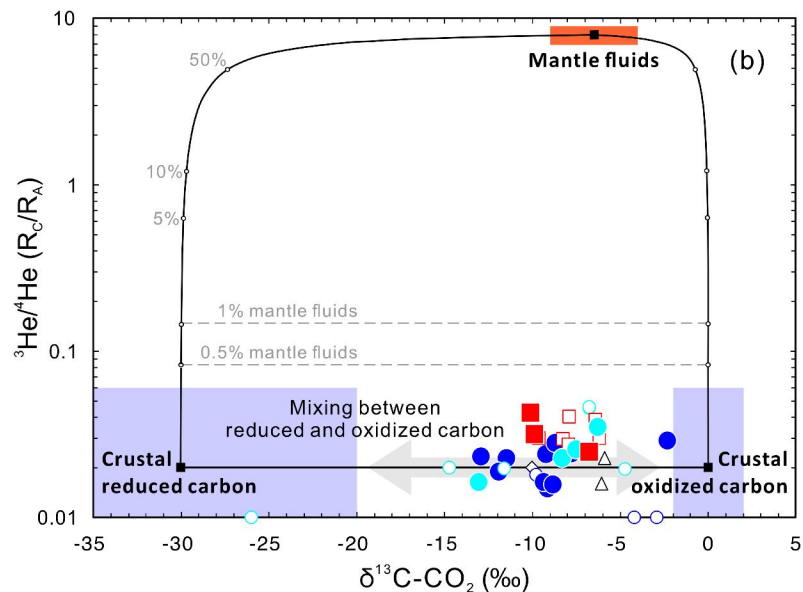
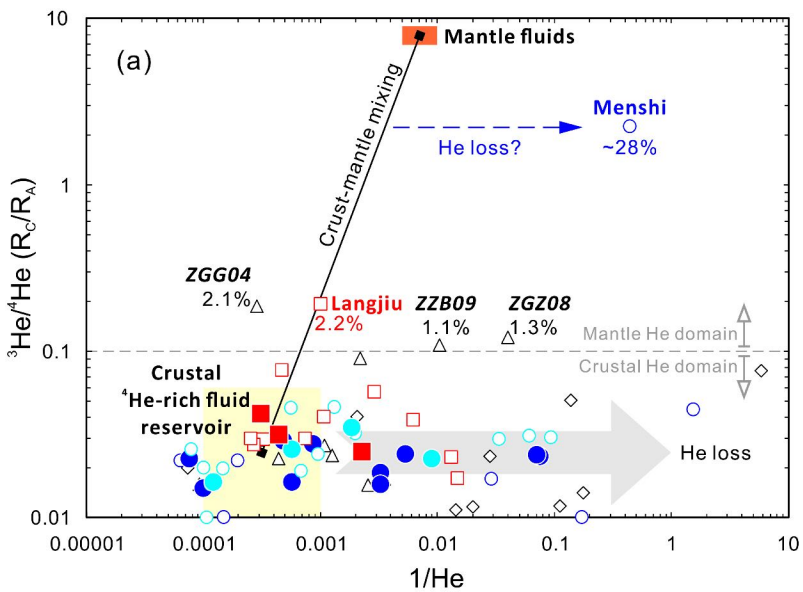


Figure 4.

Karakoram strike-slip fault

